Journal of
Sensor and Actuator Networks

MDPI

Article

Non-Invasive Differential Temperature Monitoring Using Sensor Array for Microwave Hyperthermia Applications: A Subspace-Based Approach

Ji Wu [1], Fan Yang [2,3], Jinchuan Zheng [1], Hung T. Nguyen [1] and Rifai Chai [1,*]

[1] School of Science, Computing and Engineering Technologies, Swinburne University of Technology, Hawthorn, VIC 3122, Australia; jwu1@swin.edu.au (J.W.); jzheng@swin.edu.au (J.Z.); hungnguyen@swin.edu.au (H.T.N.)
[2] Sichuan Canyearn Medical Equipment Co., Ltd., Chengdu 610000, China; yangfan@wpeony.com
[3] Shenzhen Peini Digital Technology Co., Ltd., Shenzhen 518000, China
* Correspondence: rchai@swin.edu.au

Abstract: Non-invasive temperature monitoring is highly valuable in applications such as microwave hyperthermia treatment, where overheating may damage healthy tissue. This paper presents a subspace-based method for real-time temperature monitoring using a sensor array configuration. The proposed method improves upon the conventional Born approximation (BA) approach by accurately estimating the total field through primary induced currents. The temperature-dependent dielectric properties of breast tissues are modeled using data from porcine tissues, and a sigmoid function is employed to create realistic temperature transition zones in the numerical breast phantom. The method is validated through extensive simulations under noise-free and noisy conditions (SNR = 30 dB and 20 dB). The results demonstrate that our method maintains consistent performance across different temperature levels (38–45 °C), achieving reconstruction accuracy within ±0.2 °C at SNR = 30 dB and ±0.5 °C at SNR = 20 dB. While the computational overhead of calculating primary induced currents slightly increases the overall processing time, it leads to a faster convergence in the cost function minimization. These findings suggest that the proposed method offers a promising solution for real-time temperature monitoring in microwave hyperthermia applications.

Keywords: non-invasive sensing; temperature monitoring; microwave hyperthermia; born approximation; subspace-based method; permittivity measurement

Academic Editor: Mário Alves

Received: 31 December 2024
Revised: 5 February 2025
Accepted: 8 February 2025
Published: 11 February 2025

Citation: Wu, J.; Yang, F.; Zheng, J.; Nguyen, H.T.; Chai, R. Non-Invasive Differential Temperature Monitoring Using Sensor Array for Microwave Hyperthermia Applications: A Subspace-Based Approach. *J. Sens. Actuator Netw.* **2025**, *14*, 19. https://doi.org/10.3390/jsan14010019

1. Introduction

Breast cancer remains one of the most prevalent malignancies among women worldwide [1], underscoring the necessity for improved diagnostic and treatment-monitoring techniques. Conventional breast imaging modalities such as X-ray mammography and magnetic resonance imaging (MRI) have significantly enhanced early detection. However, these technologies can be costly, require specialized infrastructure, and involve ionizing radiation in the case of mammography. An emerging and potentially transformative alternative is microwave imaging, which uses low-power electromagnetic waves in the microwave frequency range to probe the dielectric properties of breast tissue [2–4]. By arranging sensors array around the breast and measuring the scattered signals at multiple angles and frequencies, microwave tomography reconstructs spatial maps of the breast's electrical properties. These maps can then serve as functional images, potentially revealing malignant lesions or physiological changes correlated with disease progression [5–7].

In recent years, there has been growing interest in leveraging microwave imaging for temperature monitoring in cancer therapy [8–12]. Two prominent treatment modalities—microwave hyperthermia [13,14] and microwave ablation [15]—rely on the controlled heating of cancerous tissue to eradicate or sensitize tumor cells. Hyperthermia treatments typically heat tissue to approximately 40–45 °C to increase tumor susceptibility to radiation or chemotherapy, while ablation procedures target temperatures exceeding 60 °C to kill tumor cells directly. Both scenarios demand accurate, fast temperature feedback to ensure effective heat delivery and to mitigate the damage to the surrounding healthy tissue. Additionally, the inherent metabolic and vascular changes in malignant tissue frequently generate localized increases in temperature, rendering it a possible diagnostic marker [16].

Thermal monitoring techniques can be broadly categorized into passive and active methods. Passive techniques, such as infrared (IR) thermography, rely on detecting the natural emission from heated surfaces and are thus confined to superficial tissues [17]. Active techniques, such as MR thermometry, exploit changes in proton resonance frequency to provide accurate volumetric temperature measurements. However, MRI systems are expensive, scarce, and unsuitable for continuous bedside or intraoperative monitoring [18,19]. Alternatively, microwave imaging circumvents these limitations by sending controlled electromagnetic signals into tissue to sense internal dielectric changes arising from temperature variations [8–12].

A key factor for microwave-based thermal monitoring is that biological tissues' dielectric properties (permittivity and conductivity) exhibit measurable change with temperature [20,21]. Compared to healthy structures like adipose tissue, tumors often contain higher water and ionic content, resulting in different baseline dielectric profiles and more pronounced temperature-related changes [22]. These temperature-dependent contrasts can be captured via an active microwave imaging approach, where one or more antennae transmit low-power microwaves into the tissue while other antennae measure the scattered fields. The collected signals encode information about both the spatial permittivity distributions and their temperature-induced variations. The ability to reconstruct these changes holds promise for non-invasive, volumetric thermometry in real time, an attractive feature for clinical hyperthermia and ablation monitoring.

Recent efforts in microwave tomography for breast hyperthermia and other thermal therapies underscore both the promise and challenges of achieving quantitative, real-time temperature monitoring. Ref. [9] demonstrates a precomputed Born approximation (BA) linear inverse-scattering solution for the real-time 3D imaging of the differential temperature, achieving a 1 frame/s refresh rate and 1 °C resolution on the water and simple model. Meanwhile, in Ref. [10], a Born iterative method (BIM) with Tikhonov regularization is introduced for the differential imaging of breast phantoms, showing that a large-scale computational approach can resolve the temperature with an accuracy of up to 3 °C (at 30 dB SNR) and 0.1 °C (at 60 dB SNR). To address the need for more precise reconstructions, more works employ distorted Born approximation (DBA) as an inverse solver [11]. To further improve the reconstruction fidelity, Ref. [12] employs a nonlinear distorted Born iterative method (DBIM) accelerated by GPUs, thereby reducing average temperature-estimation errors from 2.5 °C to 1.0 °C under noise-free conditions. Based on prior research in microwave hyperthermia thermal monitoring, there are three key design criteria for a temperature-monitoring algorithm. First, it must offer sufficient accuracy in both temperature estimation and localization to ensure the effective heating of the target area and prevent damage to healthy tissue. Second, the computation time must be minimal, as delayed feedback can lead to excessive or uncontrolled heating. Finally, the algorithm must exhibit high noise robustness, maintaining reasonable accuracy even under the real-world noise conditions typical of practical imaging systems.

Following the mentioned design standards, this paper presents an approach based on a subspace-based method for non-invasive thermal variation monitoring in breast hyperthermia. In BA and DBA, the secondary incident field are used to approximate the total electric field, considering the scattered signals from the scatterer are relatively small. To improve the total field approximation, the deterministic induced current [23,24] is employed in the imaging process. Considering the relatively small variations in dielectric properties and inspired by our previous work [23], the Green's function remains unchanged in our proposed 2D method. The cost function is minimized using Tikhonov regularization and the TwIST algorithm. A 2D breast model is employed to validate the feasibility of the proposed method. Different from our previous work [23], which focused on general microwave imaging reconstruction, this paper extends the subspace-based method specifically for temperature monitoring in hyperthermia applications. We implement multi-frequency data acquisition to enhance thermal monitoring under different noise conditions, and a sigmoid-based temperature transition model is introduced to simulate realistic thermal distributions in tissue. These improvements enable accurate temperature monitoring with reconstruction errors within ±0.2 °C at SNR = 30 dB and ±0.5 °C at SNR = 20 dB. The remainder of this paper is organized as follows: Section 2.1 presents the formulation of both forward and inverse solvers; Section 2.2 describes the breast model and heating model used in the validation; Section 3.1 demonstrates and discusses the differences between the proposed method and the BA-based approach in a noise-free environment; Section 3.2 further illustrates and discusses the performance of the algorithm under different noise levels; and Section 4 concludes the paper.

2. Methods

2.1. Subspace-Based Temperature-Monitoring Algorithm

2.1.1. Forward Solver

Figure 1 illustrates the 2D setup for the microwave imaging problem: the scatterer is placed in the domain of interest (DOI) D, while a set of sensors on a circular boundary denotes the locations S of transmitter and receiver antennae. Each transmitter illuminates the domain with an incident wave, and the forward solver calculates the total electric field throughout D. After enough time steps, the fields reach a steady state, and the scattered signals collected at the receiver antennae are then used for the inverse problem.

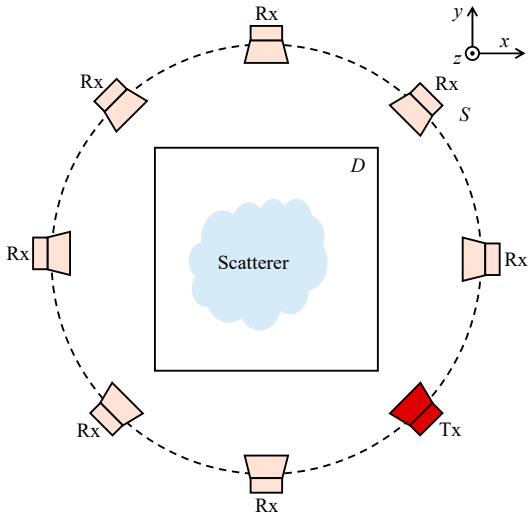

Figure 1. 2D configuration of the EM scattering problem. The circular sensors array is located outside the domain of interest D. Tx and Rx represent the transmitter and receiver.

To simulate the measurement data, we use the Finite-Difference Time-Domain (FDTD) method, which is an approach that models electromagnetic wave propagation by discretizing Maxwell's equations in both space and time. This method updates electric and magnetic field components at successive time steps on a structured grid [25]. By specifying material properties (such as permittivity and conductivity) and boundary conditions, FDTD computes the total field at each point in the DOI. Considering a 2D transverse magnetic mode in the z-axis (TM_Z) scenario, the total field satisfies the following equation:

$$\boldsymbol{E}^{tot}(\mathbf{r},\mathbf{r}'';\omega) = \boldsymbol{E}^{inc}(\mathbf{r},\mathbf{r}';\omega) + \int_D \boldsymbol{G}(\mathbf{r}'',\mathbf{r};\omega)\cdot\boldsymbol{\chi}(\mathbf{r};\omega)\cdot\boldsymbol{E}^{tot}(\mathbf{r},\mathbf{r}';\omega), \tag{1}$$

where $\boldsymbol{E}^{tot}$ and $\boldsymbol{E}^{inc}$ represent the total electric field and incident field. The vector $\mathbf{r} \in D$ denotes the source point in the domain D. The vectors $\mathbf{r}' \in S$ and $\mathbf{r}'' \in S$ denote the location of the transmitters and receivers outside the DOI. The contrast function was defined as $\boldsymbol{\chi}(\mathbf{r};\omega) = \varepsilon_r(\mathbf{r})/\varepsilon_b - 1 - j(\sigma(\mathbf{r}) - \sigma_b)/\omega\varepsilon_b$, where $\varepsilon_r(\mathbf{r})$ and $\sigma(\mathbf{r})$ represent the relative permittivity and conductivity at position $\mathbf{r}$. Then, ε_b and σ_b represent the background medium permittivity and conductivity, respectively. At last, ω represents the angular frequency. The Green's function for the background is expressed as follows:

$$\boldsymbol{G}(\mathbf{r}'',\mathbf{r};\omega) = -\frac{jk_b^2}{4}H_0^{(2)}(k_b|\mathbf{r}-\mathbf{r}''|), \tag{2}$$

where k_b is the wavenumber in the background. In Equation (2), $H_0^{(2)}$ represents the Hankel function of the second kind of order zero. Once the total field is computed, the scattered field on $\mathbf{r}''$ outside the domain D satisfies the following integral equation:

$$\boldsymbol{E}^{sca}(\mathbf{r}',\mathbf{r}'';\omega) = \int_D \boldsymbol{G}(\mathbf{r}'',\mathbf{r};\omega)\cdot\boldsymbol{\chi}(\mathbf{r};\omega)\cdot\boldsymbol{E}^{tot}(\mathbf{r},\mathbf{r}';\omega). \tag{3}$$

If the domain D is discretized into N_i subunits, Equations (1) and (2) can be expressed in the following compact form:

$$\boldsymbol{E}^{tot} = (\boldsymbol{I} - \boldsymbol{G}_D\cdot\boldsymbol{\chi})^{-1}\cdot\boldsymbol{E}^{inc}, \tag{4}$$

$$\boldsymbol{E}^{sca} = \boldsymbol{G}_S\cdot\boldsymbol{\chi}\cdot(\boldsymbol{I} - \boldsymbol{G}_D\cdot\boldsymbol{\chi})^{-1}\cdot\boldsymbol{E}^{inc}, \tag{5}$$

where $\boldsymbol{G_D}$ and $\boldsymbol{G_S}$ are Green's function operators obtained from Equation (2) and $\boldsymbol{I}$ is the identity matrix.

In this study, the breast is embedded in Domain D, surrounded by 30 antennae arranged uniformly in a circle with a 10 cm radius, each separated by 12°. All antennae function as receivers, while 10 of them are selected as transmitters, evenly spaced at 36° intervals. Each antenna is treated as a line source within the FDTD scheme. When one transmitter is transmitting, the remaining antennae act as receivers, leading to a total of N_t = 10 transmitters and N_r = 30 receivers. To enhance imaging performance, we collect multi-frequency data at 800 MHz, 1.1 GHz, and 1.5 GHz.

2.1.2. Inverse Solver

In the BA or DBA, the total field is approximated using the secondary incident field derived from an inhomogeneous background, which adopts field-based information only. By contrast, approaches like contrast source inversion (CSI) [26] and the subspace optimization method (SOM) [23,24] employ the Green's function operator and scattered field to recover the induced current. The key distinction is that CSI treats the entire induced

current as a single quantity, whereas SOM divides it into primary and secondary parts. In this study, we adopt a total field approximation expressed as follows:

$$\boldsymbol{E}^{tot} = \boldsymbol{E}^{bac} + \boldsymbol{G}_{bD} \cdot \boldsymbol{C}, \tag{6}$$

where $\boldsymbol{E}^{bac}$ denotes the secondary incident field which can be computed using Equation (4) by substituting $\boldsymbol{E}^{tot}$ with $\boldsymbol{E}^{bac}$. The secondary incident field $\boldsymbol{E}^{bac}$ is obtained using the contrast of the image domain at normal temperature (37 °C), without accounting for temperature changes. The vector $\boldsymbol{C}$ denotes the induced current that is generated from the differential contrast $\Delta\boldsymbol{\chi}$ between the contrast of the heated image domain and the contrast of the image domain at normal temperature $\boldsymbol{\chi}$, which is expressed as $\boldsymbol{C} = \Delta\chi \cdot \boldsymbol{E}^{tot}$. When $\boldsymbol{C} = 0$, it is a special case of BA. The Green's function operator of inhomogeneous background is obtained as follows:

$$\boldsymbol{G}_{bS} = \boldsymbol{G}_S \cdot (\boldsymbol{I} - \boldsymbol{\chi} \cdot \boldsymbol{G}_D)^{-1}, \tag{7}$$

$$\boldsymbol{G}_{bD} = \boldsymbol{G}_D \cdot (\boldsymbol{I} - \boldsymbol{\chi} \cdot \boldsymbol{G}_D)^{-1}. \tag{8}$$

Because noise is unavoidable in real-world measurements, the induced current can be divided into two parts: a primary induced current that contains the main scatterer information and a secondary induced current that primarily represents noise. We perform singular value decomposition (SVD) on the inhomogeneous Green's equation, leading to the following:

$$\begin{gathered} \boldsymbol{G}_{bS} = \sum \boldsymbol{u}_i \sigma_i \boldsymbol{v}_i^*, \\ \sigma_1 \geq \sigma_2 \geq \cdots \geq \sigma_{N_r} \geq 0. \end{gathered} \tag{9}$$

From this SVD-based relationship, we can then compute the induced current as follows:

$$\boldsymbol{C} = \sum_{i=1}^{L} \frac{\boldsymbol{u}_i^* \cdot \left(\boldsymbol{E}^{sca} - \boldsymbol{G}_S \cdot \boldsymbol{\chi} \cdot \boldsymbol{E}^{bac} \right)}{\sigma_i} \cdot \boldsymbol{v}_i, \tag{10}$$

where L is defined as the number of primary singular values within $[0, N_r]$. By using the first L singular values to compute the primary induced current, we retain the main scattering information of the object while suppressing noise associated with the secondary induced current, which greatly enhances the noise robustness of our method. The optimal performance is typically achieved if the L-th singular value σ_L is approximately 50% of the first singular value σ_1. In this work, L is empirically chosen as 15, which provides a better trade-off between retrieving a sufficient volume of primary induced current and suppressing noise.

Based on the theoretical framework described above, the microwave temperature-monitoring problem can be formulated as a linear inverse problem of the form $\boldsymbol{y} = \boldsymbol{A}\boldsymbol{x}$, where $\boldsymbol{y}$ is the observation vector, $\boldsymbol{x}$ represents the optimal dielectric property changes vector, and $\boldsymbol{A}$ is the inverse operator. The Two-step Iterative Shrinkage/Thresholding (TwIST) algorithm is designed for solving ill-posed linear inverse problems that arise in image restoration and reconstruction applications. Unlike the traditional Iterative Shrinkage/Thresholding algorithm, TwIST employs a two-step iteration scheme that updates the current solution using information from both the previous and current iterations:

$$\boldsymbol{x}_{k+1} = (1 - \alpha)\boldsymbol{x}_{k-1} + (\alpha - \beta)\boldsymbol{x}_k + \beta\Gamma_\lambda(\boldsymbol{x}_k), \tag{11}$$

where $\boldsymbol{x}_k$ represents the solution at the k-th iteration, α and β are convergence control parameters, and $\Gamma_\lambda(\boldsymbol{x}_k)$ is a denoising operator to stabilize the optimization [27]. This two-step approach significantly improves convergence speed compared to standard one-step iterations, especially for ill-conditioned problems. To estimate $\boldsymbol{x}$ from the observation

data, we construct a cost function that minimizes the mismatch between the measured and calculated scattered signals:

$$F(\Delta\chi) = \| \boldsymbol{E}^{sca} - \boldsymbol{G}_S \cdot \chi \cdot \boldsymbol{E}^{bac} - \boldsymbol{G}_{bS} \cdot \Delta\chi \cdot \boldsymbol{E}^{tot} \|^2 + \gamma \|\Delta\chi\|^2, \quad (12)$$

where γ is the parameter of Tikhonov regularization [28], which is empirically determined.

Solving this optimization problem by subspace-based TwIST (S-TwIST), as proposed in our previous work [23], yields the dielectric property changes $\Delta\chi$, which can then be converted to temperature variations within the breast model.

2.1.3. Temperature-Dependent Dielectric Properties of Breast Tissue

Although it is well-known that tissue dielectric properties are temperature-dependent, to the best of our knowledge, no study has provided an experimental model of temperature-dependent dielectric properties specifically for human breast tissue. Some works instead utilize animal tissue measurements as substitutes. Since water content is the primary determinant of tissue dielectric properties, we use this criterion to match suitable animal tissue models to human breast tissue in our study. For instance, [21] investigates porcine tissue and provides Cole–Cole parameters as temperature polynomials, reporting parameters for porcine liver, muscle, fat, and blood tissues.

Among these models, this paper focuses on the liver, fat, and blood data. Liver tissue serves as an analog to breast glandular tissue due to their similar high water content. While breast tumors also exhibit high water content, they typically show increased vascularization compared to normal tissue due to abnormal metabolism [29], making their characteristics closely aligned with blood, consistent with observations in [30]. Similarly, both fat tissue and breast adipose tissue are categorized as low water content tissues. Therefore, we adopt the temperature-dependent dielectric data from porcine liver, fat, and blood in [21] as substitutes for breast glandular tissue, breast adipose, and tumors, respectively. Figure 2 illustrates the temperature-dependent dielectric properties of pig liver, fat, and blood as reported in [21].

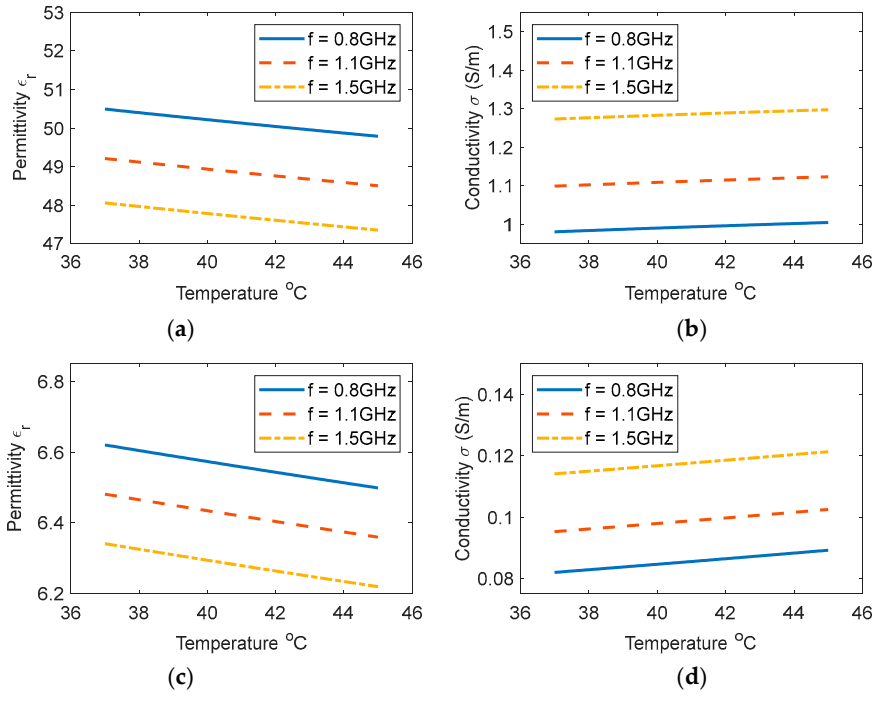

Figure 2. *Cont.*

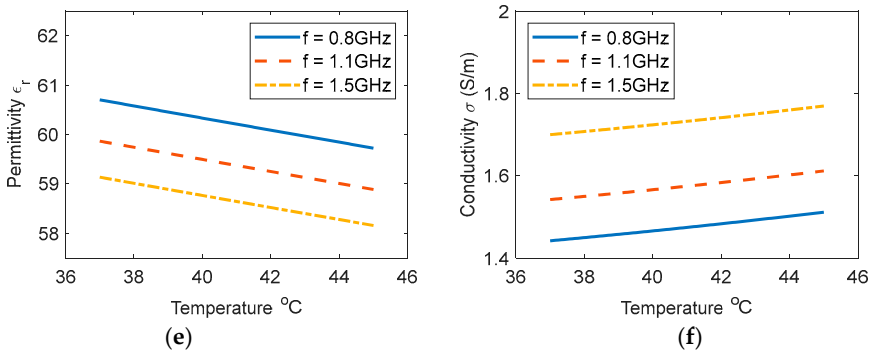

Figure 2. Temperature-dependent dielectric properties of porcine tissues at three specific frequencies: (**a**) relative permittivity of liver versus temperature, (**b**) conductivity of liver versus temperature, (**c**) relative permittivity of fat versus temperature, (**d**) conductivity of fat versus temperature, (**e**) relative permittivity of blood versus temperature, and (**f**) conductivity of blood versus temperature.

As shown in Figure 2, the relationship between temperature and dielectric properties is approximately linear in the range of 37 °C to 45 °C. Specifically, relative permittivity decreases with increasing temperature, while conductivity shows a positive correlation. For simplicity, we adopt a linear approximation similar to [10]. In Figure 2, the permittivity and conductivity variations with temperature are presented for three tissue types: liver, fat, and blood. As the temperature increases from 37 °C to 45 °C, permittivity decreases by 1.68% (Figure 2a), 2.15% (Figure 2c), and 1.98% (Figure 2e). Similarly, conductivity increases by 6.44% (Figure 2b), 8.81% (Figure 2d), and 7.87% (Figure 2f). Based on the trends observed in Figure 2, the temperature–permittivity coefficient is −0.25%, meaning that permittivity decreases by 0.25% for every 1 °C increase relative to 37 °C. Likewise, the temperature–conductivity coefficient is +1%, meaning that conductivity increases by 1% for every 1 °C increase relative to 37 °C.

Using this linear relationship, we can determine the temperature variation ΔT from the dielectric property changes $\Delta\chi$ obtained through our inverse solver. Specifically, we have the following:

$$\Delta T(\mathbf{r}) = -\frac{\left(\frac{Re\{\Delta\chi(\mathbf{r})\}}{Re\{\chi(\mathbf{r})\}}\right)}{0.25\%} = -400\left(\frac{Re\{\Delta\chi(\mathbf{r})\}}{Re\{\chi(\mathbf{r})\}}\right), \tag{13}$$

$$\Delta T(\mathbf{r}) = \frac{\left(\frac{Im\{\Delta\chi(\mathbf{r})\}}{Im\{\chi(\mathbf{r})\}}\right)}{1\%} = 100\left(\frac{Im\{\Delta\chi(\mathbf{r})\}}{Im\{\chi(\mathbf{r})\}}\right), \tag{14}$$

where $Re\{\cdot\}$ and $Im\{\cdot\}$ denote the real part and imaginary part of a complex value.

In order to evaluate the performance of the proposed method, the error function is constructed as the relative error of the true temperature variation distribution and recovered temperature variation distribution.

$$\xi_T = \frac{\| T_{true} - T_{recovered} \|^2}{\| T_{true} \|^2}. \tag{15}$$

2.2. Model Parameters

2.2.1. Digital Breast Model

This study employs the MRI-derived breast model from the UWCEM Numerical Breast Phantom Repository [31]. Specifically, we utilize the 125th vertical cross-section from the heterogeneously dense model (breast ID: 070604PA2). Figure 3 illustrates the distributions of relative permittivity and conductivity for this cross-section.

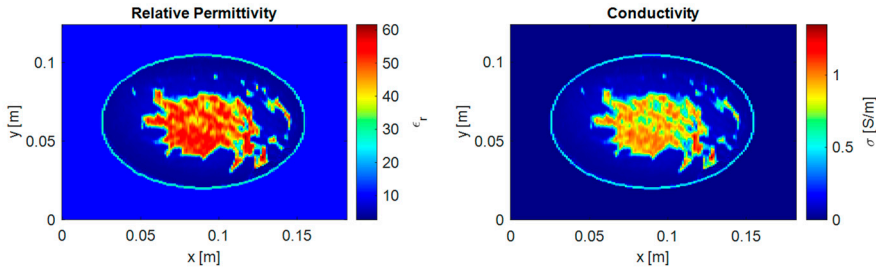

Figure 3. The dielectric properties of the 2D cross-section from the selected digital breast model (breast ID: 070604PA2).

A high-resolution digital breast model with 1 mm resolution is employed for the forward solver to obtain accurate scattered field measurements. In the inverse solver, the model is down-sampled to 2 mm resolution. This coarser resolution serves two purposes: preventing inverse crime (i.e., using identical models in both forward and inverse solvers) and reducing computational complexity during reconstruction.

Within the breast model, conductivity and relative permittivity exhibit a strong correlation. While [32] employs a single-pole Debye model to describe this relationship, we adopt a simpler linear approximation to reduce computational complexity. Through linear regression analysis of the breast tissue dielectric properties, we establish the following relationship between relative permittivity and conductivity:

$$\sigma(\varepsilon_r) = 0.0190\varepsilon_r - 0.0505, \tag{16}$$

where σ is the conductivity, and ε_r is the relative permittivity. This linear approximation provides computational efficiency while maintaining sufficient accuracy for microwave imaging applications. Notably, under this approximation, the temperature variation is determined from the change in relative permittivity.

A circular tumor of 7.5 mm radius is placed at position $(-15, 0)$ mm, as illustrated in Figure 4. The frequency-dependent relative permittivity of the breast tumor is described by the ex vivo model in [30]. Combined with the temperature-dependent dielectric properties of porcine blood mentioned above, the tumor's dielectric properties in this study are established according to Figure 2e.

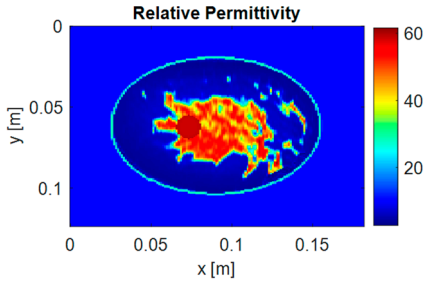

Figure 4. The relative permittivity distribution of the selected digital breast (breast ID: 070604PA2) with tumor.

2.2.2. Heating Model

A sigmoid function is employed to simulate the heating process and create smooth temperature transitions at the heating boundaries, as shown in Figure 5. Using the tumor center as the origin, the heated region has a radius of $0.5R_a$, where R_a denotes the tumor radius. A transition zone is defined as an annular region with inner radius $0.5R_a$ and outer radius $1.25R_a$. All regions beyond $1.25R_a$ from the heating center maintain a baseline

temperature of 37 °C. In this study, the heating process increases the temperature from 37 °C to 45 °C in 1 °C increments.

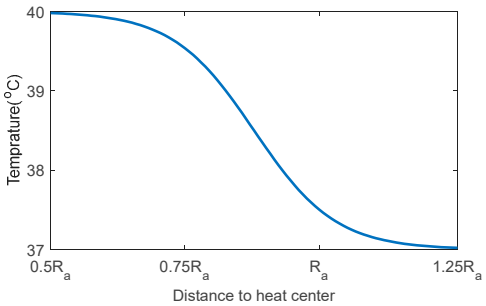

Figure 5. The sigmoid function used for modelling temperature transition, where the horizontal axis represents the distance from the heating center and the vertical axis represents the temperature.

Taking the case of 40 °C heating as an example, we have the following: Figure 6a shows the relative permittivity distribution of the heated breast phantom, Figure 6b illustrates the temperature distribution across the imaging domain, where the central heated region maintains a uniform temperature of 40 °C while the transition zone exhibits a smooth temperature decrease to 37 °C with increasing distance from the center. The implementation of such transition zones is supported by previous heating studies using breast phantoms [10,33]. Figure 6c demonstrates the resulting changes in relative permittivity across the imaging domain due to this heating pattern.

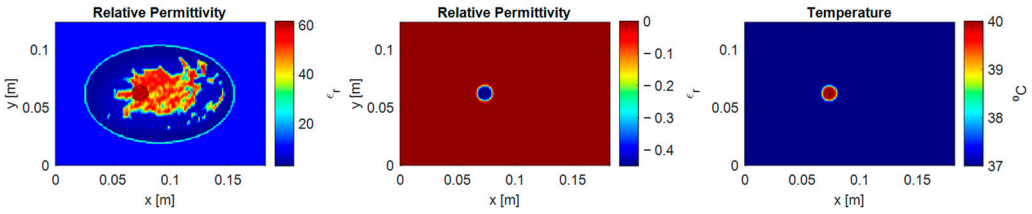

(**a**) (**b**) (**c**)

Figure 6. Heating effects at 40 °C: (**a**) relative permittivity distribution of the heated digital breast, (**b**) changes in relative permittivity due to heating, and (**c**) temperature distribution across the imaging domain.

Based on the digital breast phantom and heating configuration described above, we conducted a series of simulations to evaluate the performance of our proposed method. The following section demonstrates the reconstruction results in an ideal noise-free scenario, followed by a comprehensive analysis under different noise conditions.

3. Results

3.1. Noise-Free Scenario

This section presents the temperature reconstruction results obtained from the BA algorithm and our proposed method. We first evaluate the performance under ideal noise-free conditions, followed by an analysis under different noise levels.

To evaluate the reconstruction accuracy, we compare the temperature distributions reconstructed by the BA algorithm and our proposed method for heating temperatures ranging from 38 °C to 45 °C in 1 °C increments. Figure 7 shows the reconstructed temperature distributions at selected temperatures for both methods.

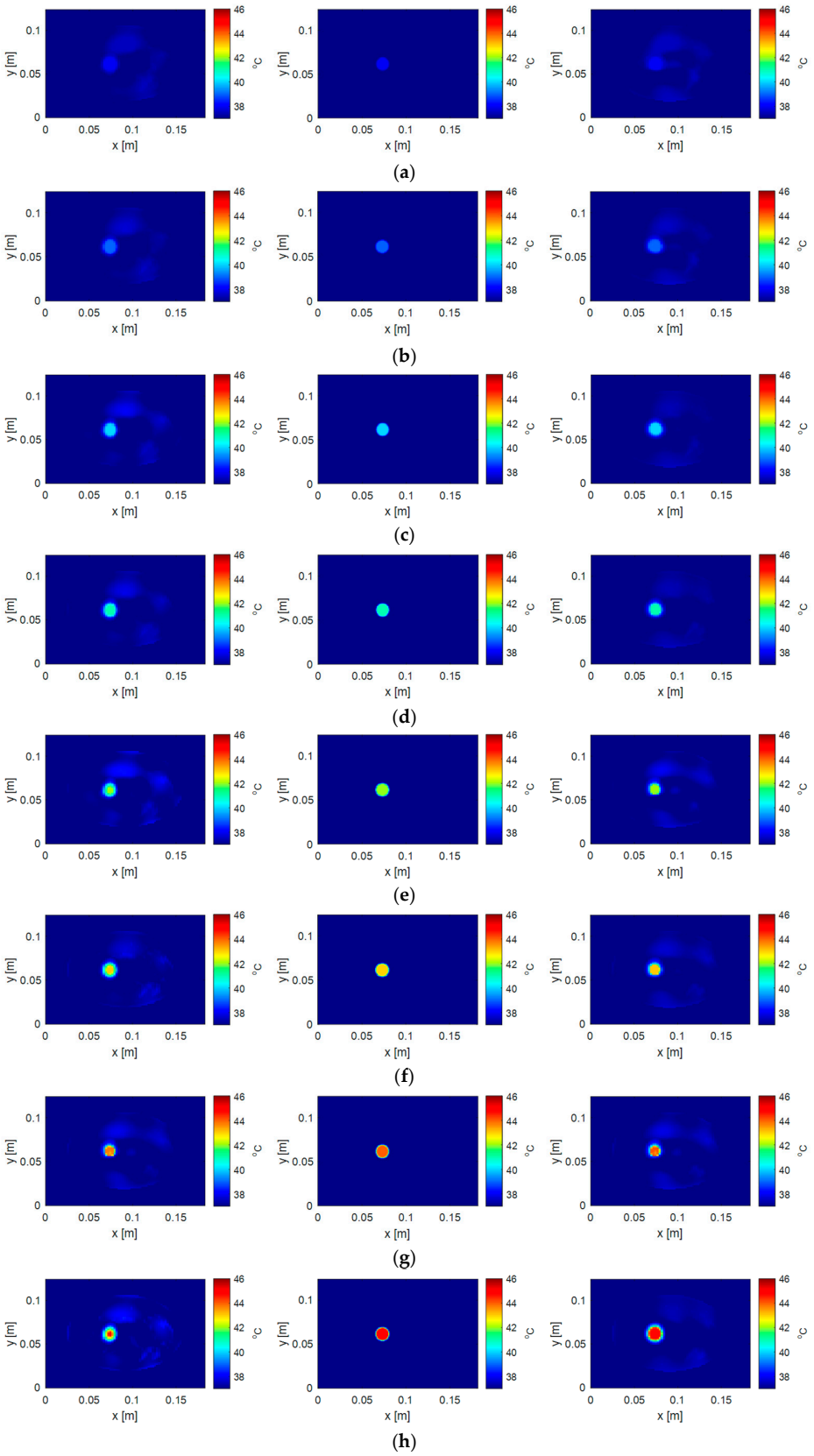

Figure 7. Comparison of temperature reconstruction results at different heating levels (38–45 °C). For each temperature level (**a**–**h**), the panels show the following: temperature distribution reconstructed by the BA method (**left**), true temperature distribution (**middle**), and temperature distribution reconstructed by the proposed method (**right**). Temperature values are indicated by the color bar in degrees Celsius.

The temperature reconstruction accuracy is evaluated using two relative error metrics obtained from Equation (15): ξ_b and ξ_h, where the subscript b indicates values within the whole breast, and subscript h indicates values within the heated region (defined as a circular area with radius $0.5R_a$ centered at the tumor position). Table 1 compares these relative errors for both methods across different temperature levels and the mean reconstructed temperature T_h within the heated region.

Table 1. Quantitative comparison of reconstruction performance between BA method and proposed method under noise-free conditions.

Temperature	ξ_b (%)		ξ_h (%)		T_h (°C)	
	BA	Proposed Method	BA	Proposed Method	BA	Proposed Method
38	0.1027	0.1027	0.2749	0.3073	38.0077	38.0313
39	0.1895	0.1916	0.2917	0.3008	39.0155	39.0626
40	0.1941	0.2601	0.3725	0.2746	40.0232	40.0232
41	0.3436	0.4932	0.3474	0.2739	41.0310	41.1252
42	0.8857	1.8057	0.4957	0.3888	42.0387	42.0500
43	1.5623	1.5618	0.3629	0.3522	43.0465	43.1878
44	2.3441	2.7092	0.4266	0.4134	43.7754	44.0542
45	3.5679	0.7262	0.5374	0.4365	45.0620	45.0620

3.2. Noisy Scenario

To evaluate the robustness of both methods in practical applications, we examine their performance under two different noise levels: SNR = 30 dB and SNR = 20 dB. White Gaussian noise is added to the scattered field measurements to simulate realistic measurement conditions.

Figures 8 and 9 present the reconstructed temperature distributions under SNR = 30 dB and SNR = 20 dB, respectively, for temperatures ranging from 38 °C to 45 °C in 1 °C increments. Tables 2 and 3 summarize the quantitative results for the two noise levels, including the relative error across the entire breast ξ_b, the relative error within the heated region ξ_h, and the reconstructed mean temperatures within the heated region T_h.

Table 2. Quantitative comparison of reconstruction performance between BA method and proposed method under SNR = 30 dB.

Temperature	ξ_b (%)		ξ_h (%)		T_h (°C)	
	BA	Proposed Method	BA	Proposed Method	BA	Proposed Method
38	0.1027	0.1027	0.3599	0.3813	38.0313	38.0077
39	0.1656	0.2010	0.3829	0.4055	39.0626	39.0155
40	0.1592	0.2503	0.3393	0.4268	40.0939	40.0232
41	0.4319	0.2237	0.5252	0.3478	41.1252	41.0310
42	1.7512	0.4190	0.5264	0.4996	42.1565	42.0387
43	1.7843	0.9560	0.4905	0.5445	43.1878	43.0465
44	3.3100	1.4657	0.5038	0.4711	44.2191	43.8342
45	5.2054	2.7036	0.5776	0.5869	44.7899	44.9820

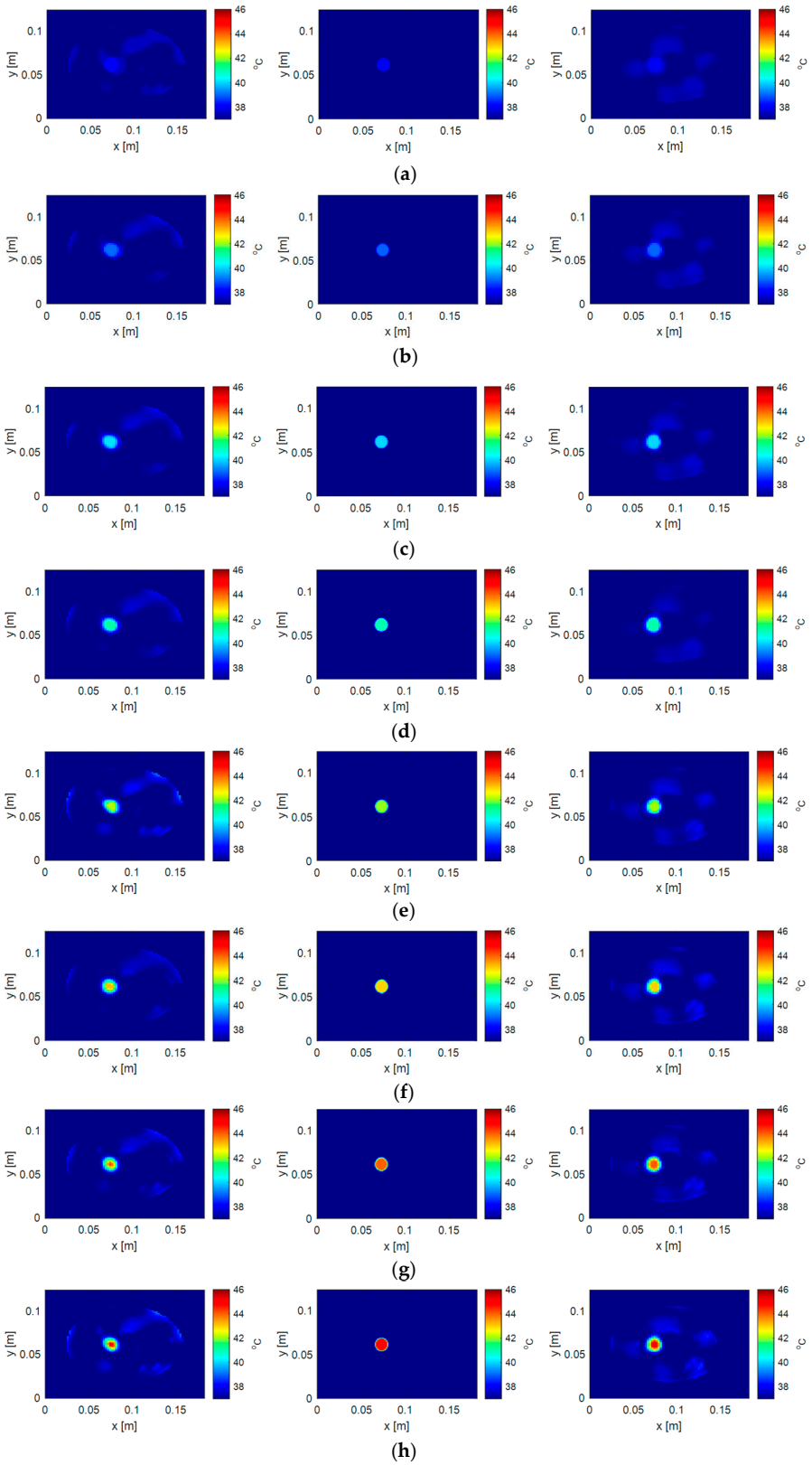

Figure 8. Comparison of temperature reconstruction results at different heating levels (38–45 °C) under SNR = 30 dB. For each temperature level (**a**–**h**), the panels show the following: temperature distribution reconstructed by the BA method (**left**), true temperature distribution (**middle**), and temperature distribution reconstructed by the proposed method (**right**). Temperature values are indicated by the color bar in degrees Celsius.

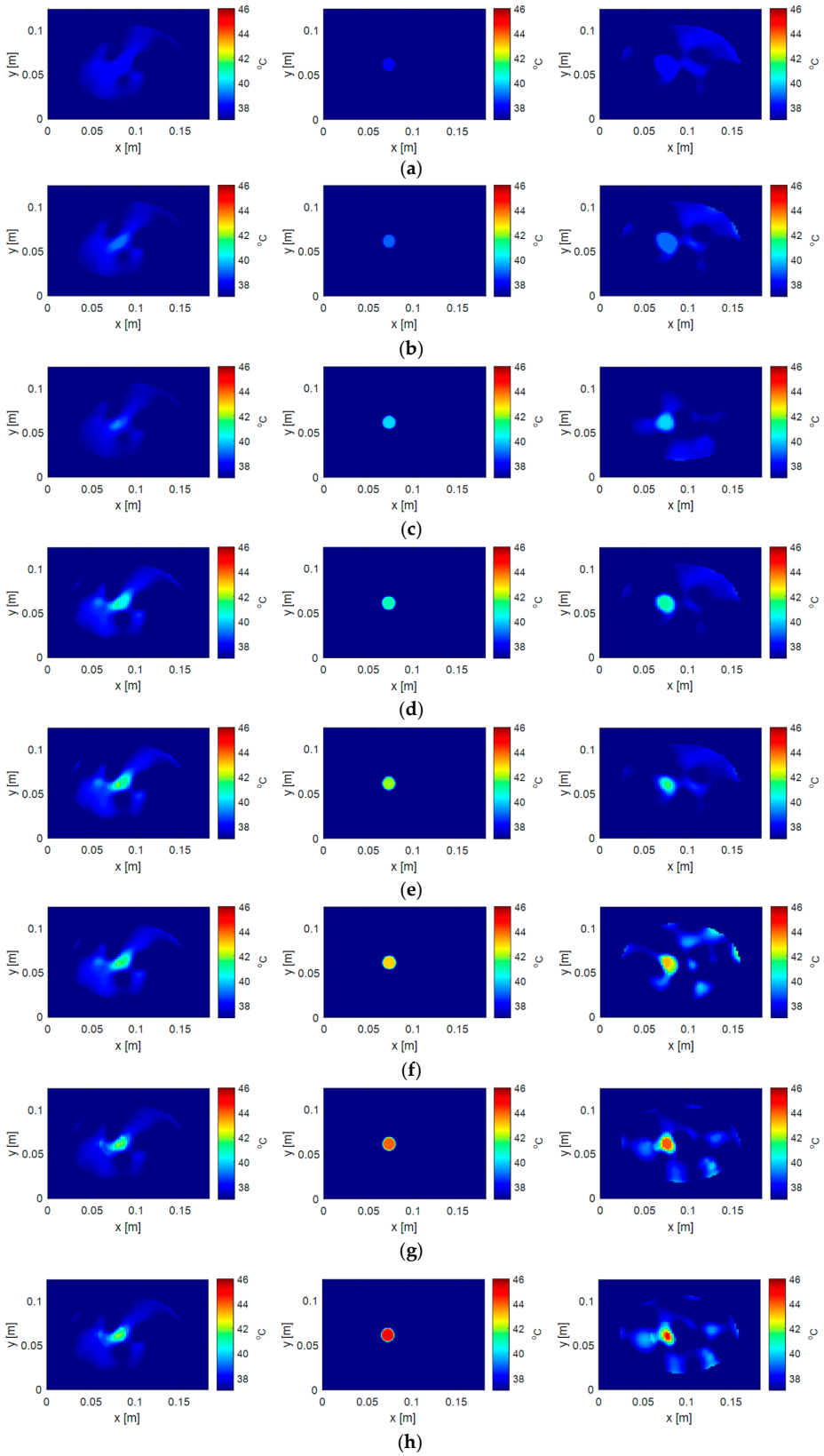

Figure 9. Comparison of temperature reconstruction results at different heating levels (38–45 °C) under SNR = 20 dB. For each temperature level (**a**–**h**), the panels show the following: temperature distribution reconstructed by the BA method (**left**), true temperature distribution (**middle**), and temperature distribution reconstructed by the proposed method (**right**). Temperature values are indicated by the color bar in degrees Celsius.

Table 3. Quantitative comparison of reconstruction performance between BA method and proposed method under SNR = 20 dB.

Temperature	ξ_b (%)		ξ_h (%)		T_h (°C)	
	BA	Proposed Method	BA	Proposed Method	BA	Proposed Method
38	0.3146	0.2940	0.7757	0.7249	38.0420	38.0077
39	0.3487	0.3503	0.8598	0.8640	39.0840	39.0155
40	3.6405	0.0956	0.7315	0.6993	39.4214	40.0232
41	3.7160	0.3526	1.2616	0.6939	41.1680	41.0400
42	5.6056	0.3091	1.3517	0.7622	42.0545	41.8240
43	7.8482	0.5785	1.3500	1.4266	41.8137	43.0600
44	9.5270	1.2706	1.0490	1.2831	42.0997	44.4700
45	11.7668	5.0855	1.0905	1.4774	42.0184	44.5433

4. Discussion

From Figure 7 and Table 1, both the BA algorithm and our proposed method demonstrate satisfactory reconstruction capabilities under noise-free conditions, with only slight performance differences. This modest improvement shown by our subspace-based approach can be attributed to two aspects: the absence of noise in the observed data benefits both reconstruction approaches, and our method's capability to estimate the total field more accurately through primary induced currents provides a slight advantage.

A notable observation is that our subspace-based algorithm maintains consistent performance across all temperature levels, while the BA method gradually degrades accuracy as temperature increases. This degradation in the BA method's performance can be explained by its fundamental assumption that the scattered field from the scatterer should be sufficiently small to approximate the total field using secondary incident fields without significant error. As the temperature rises, the changes in dielectric properties become more pronounced, challenging this underlying assumption of the BA method. These results demonstrate that our proposed method has the potential to improve upon the BA method's total field approximation, particularly in scenarios involving larger dielectric property variations.

Following the noise-free analysis, we further evaluated the robustness of both methods under different measurement conditions, and their performance at two noise levels, SNR = 30 dB and SNR = 20 dB is examined. The SNR in practical microwave imaging systems can vary significantly depending on multiple factors, including hardware design, operational frequency range, imaging parameters, and environmental conditions.

First, while the reconstructions at SNR = 30 dB closely resemble the noise-free results, those at SNR = 20 dB exhibit more artifacts and distortions, indicating an increased reconstruction difficulty with higher noise levels. For the BA method, the reconstruction accuracy significantly deteriorates at larger temperature differences. In contrast, although our subspace-based method also shows decreased accuracy, it consistently outperforms the BA method across all quantitative metrics.

Second, under SNR = 20 dB conditions, the BA method fails to accurately reconstruct temperatures above 42 °C, while our proposed method maintains an accuracy within ± 0.5 °C even at higher temperatures.

Regarding computational efficiency, while our method requires additional computational time (1.8946 s vs. 1.2943 s), this overhead is justified by the improved reconstruction accuracy. The computation consists of two components: calculating primary induced

currents (0.8318 s) and minimizing the cost function (1.0584 s). This indicates that, while computing primary induced currents adds computational overhead to the temperature-monitoring algorithm, the more accurate total field estimation leads to a faster cost function minimization process convergence.

While the proposed method shows promising results, several limitations should be acknowledged. The current study is limited to 2D reconstruction and uniform heating patterns. Additionally, the linear approximation of the temperature-dependent dielectric properties may not fully capture the complexity of biological tissue responses. Future work should address these limitations by extending to 3D reconstruction, validating the performance under non-uniform heating conditions, and incorporating more sophisticated temperature–dielectric property relationships. Furthermore, experimental validation will be essential for verifying the method's effectiveness in practical applications.

5. Conclusions

This paper presents a subspace-based temperature-monitoring method for microwave hyperthermia applications using a non-invasive sensor array. The proposed approach improves upon the Born approximation by introducing a more accurate total field estimation through primary induced currents. The method was validated using a 2D numerical breast phantom under various temperature conditions and noise levels.

The numerical results demonstrate that, in noise-free conditions, both methods show satisfactory reconstruction capabilities, while our method maintains more consistent performance across different temperature levels compared to the BA method. Under realistic noise conditions, our method achieves reconstruction accuracy within ± 0.2 °C at SNR = 30 dB and maintains accuracy within ± 0.5 °C even at SNR = 20 dB. In contrast, the BA method's performance deteriorates significantly for temperatures above 42 °C under SNR = 20 dB. Although our method requires additional computational time for calculating primary induced currents, this overhead is compensated by a faster convergence in the cost function minimization process.

Future work will focus on extending the method to 3D reconstruction, validating its performance under non-uniform heating patterns, and experimental verification using practical sensor array configurations. These developments will be crucial for implementing non-invasive microwave-based temperature monitoring in hyperthermia treatments.

Author Contributions: Conceptualization, J.W. and R.C.; methodology, J.W., F.Y. and R.C.; software, J.W.; validation, J.W. and R.C.; formal analysis, J.W., J.Z., H.T.N. and R.C.; investigation, J.W., F.Y., J.Z., H.T.N. and R.C.; resources, J.W., F.Y., J.Z., H.T.N. and R.C.; data curation, J.W.; writing—original draft preparation, J.W.; writing—review and editing, F.Y., J.Z., H.T.N. and R.C.; visualization, J.W.; supervision, F.Y., J.Z., H.T.N. and R.C. All authors have read and agreed to the published version of the manuscript.

Funding: This research received no external funding.

Data Availability Statement: This manuscript uses numerical breast phantoms from the University of Wisconsin Computational Electromagnetics Laboratory (UWCEM) Phantom Repository. The breast phantoms are publicly available at the UWCEM—Phantom Repository (https://uwcem.ece.wisc.edu/phantomRepository.html).

Conflicts of Interest: Author Fan Yang was employed by the company Shenzhen Peini Digital Technology Co., Ltd. The remaining authors declare that the research was conducted in the absence of any commercial or financial relationships that could be construed as a potential conflict of interest.

References

1. Ferlay, J.; Ervik, M.; Lam, F.; Laversanne, M.; Colombet, M.; Mery, L.; Piñeros, M.; Znaor, A.; Soerjomataram, I.; Bray, F. Global Cancer Observatory: Cancer Today (Version 1.1). Available online: https://gco.iarc.who.int/today (accessed on 19 December 2024).
2. Fear, E.C.; Hagness, S.C.; Meaney, P.M.; Okoniewski, M.; Stuchly, M.A. Enhancing breast tumor detection with Near-Field Imaging. *IEEE Microw. Mag.* **2002**, *3*, 48–56. [CrossRef]
3. Li, X.; Davis, S.K.; Hagness, S.C.; van der Weide, D.W.; Van Veen, B.D. Microwave imaging via space-time beamforming: Experimental investigation of tumor detection in multilayer breast phantoms. *IEEE Trans. Microw. Theory Tech.* **2004**, *52*, 1856–1865. [CrossRef]
4. Meaney, P.M.; Fanning, M.W.; Li, D.; Poplack, S.P.; Paulsen, K.D. A clinical prototype for active microwave imaging of the breast. *IEEE Trans. Microw. Theory Tech.* **2000**, *48*, 1841–1853. [CrossRef]
5. Pastorino, M. Applications of Microwave Imaging. In *Microwave Imaging*; Wiley: Hoboken, NJ, USA, 2010; pp. 229–263.
6. Golnabi, A.H.; Meaney, P.M.; Epstein, N.R.; Paulsen, K.D. Microwave Imaging for Breast Cancer Detection: Advances in Three-Dimensional Image Reconstruction. In Proceedings of the 2011 Annual International Conference of the IEEE Engineering in Medicine and Biology Society, Boston, MA, USA, 30 August–3 September 2011; pp. 5730–5733.
7. Fear, E.C.; Bourqui, J.; Curtis, C.; Mew, D.; Docktor, B.; Romano, C. Microwave Breast Imaging With a Monostatic Radar-Based System: A Study of Application to Patients. *IEEE Trans. Microw. Theory Tech.* **2013**, *61*, 2119–2128. [CrossRef]
8. Nguyen, P.T.; Abbosh, A.M.; Crozier, S. 3-D Focused Microwave Hyperthermia for Breast Cancer Treatment with Experimental Validation. *IEEE Trans. Antennas Propag.* **2017**, *65*, 3489–3500. [CrossRef]
9. Haynes, M.; Stang, J.; Moghaddam, M. Real-time Microwave Imaging of Differential Temperature for Thermal Therapy Monitoring. *IEEE Trans. Biomed. Eng.* **2014**, *61*, 1787–1797. [CrossRef] [PubMed]
10. Onal, H.; Yilmaz, T.; Akinci, M.N. A BIM-Based Algorithm for Quantitative Monitoring of Temperature Distribution During Breast Hyperthermia Treatments. *IEEE Access* **2023**, *11*, 38680–38695. [CrossRef]
11. Lee, K.J.; Kim, J.Y.; Kim, B.R.; Jeon, S.I.; Kim, N.; Son, S.H. Real-Time 2D Microwave Differential Imaging for Temperature Monitoring. In Proceedings of the 2018 International Symposium on Antennas and Propagation (Isap), Busan, Repulic of Korea, 23–26 October 2018.
12. Chen, G.B.; Stang, J.; Haynes, M.; Leuthardt, E.; Moghaddam, M. Real-Time Three-Dimensional Microwave Monitoring of Interstitial Thermal Therapy. *IEEE Trans. Biomed. Eng.* **2018**, *65*, 528–538. [CrossRef]
13. Roemer, R.B. Engineering aspects of hyperthermia therapy. *Annu. Rev. Biomed. Eng.* **1999**, *1*, 347–376. [CrossRef] [PubMed]
14. Stauffer, P.R. Evolving technology for thermal therapy of cancer. *Int. J. Hyperth.* **2005**, *21*, 731–744. [CrossRef]
15. Schaible, J.; Pregler, B.; Bäumler, W.; Einspieler, I.; Jung, E.M.; Stroszczynski, C.; Beyer, L.P. Safety margin assessment after microwave ablation of liver tumors: Inter- and intrareader variability. *Radiol. Oncol.* **2020**, *54*, 57–61. [CrossRef] [PubMed]
16. Ferraioli, F.; Formisano, A.; Martone, R. Effective Exploitation of Prior Information in Electrical Impedance Tomography for Thermal Monitoring of Hyperthermia Treatments. *IEEE Trans. Magn.* **2009**, *45*, 1554–1557. [CrossRef]
17. Arora, N.; Martins, D.; Ruggerio, D.; Tousimis, E.; Swistel, A.J.; Osborne, M.P.; Simmons, R.M. Effectiveness of a noninvasive digital infrared thermal imaging system in the detection of breast cancer. *Am. J. Surg.* **2008**, *196*, 523–526. [CrossRef] [PubMed]
18. Rieke, V.; Butts Pauly, K. MR thermometry. *J. Magn. Reson. Imaging* **2008**, *27*, 376–390. [CrossRef] [PubMed]
19. Davis, R.M.; Viglianti, B.L.; Yarmolenko, P.; Park, J.Y.; Stauffer, P.; Needham, D.; Dewhirst, M.W. A method to convert MRI images of temperature change into images of absolute temperature in solid tumours. *Int. J. Hyperth.* **2013**, *29*, 569–581. [CrossRef] [PubMed]
20. Lazebnik, M.; Popovic, D.; McCartney, L.; Watkins, C.B.; Lindstrom, M.J.; Harter, J.; Sewall, S.; Ogilvie, T.; Magliocco, A.; Breslin, T.M.; et al. A large-scale study of the ultrawideband microwave dielectric properties of normal, benign and malignant breast tissues obtained from cancer surgeries. *Phys. Med. Biol.* **2007**, *52*, 6093–6115. [CrossRef]
21. Ley, S.; Schilling, S.; Fiser, O.; Vrba, J.; Sachs, J.; Helbig, M. Ultra-Wideband Temperature Dependent Dielectric Spectroscopy of Porcine Tissue and Blood in the Microwave Frequency Range. *Sensors* **2019**, *19*, 1707. [CrossRef]
22. Nikolova, N.K. *Introduction to Microwave Imaging*; Cambridge University Press: Cambridge, UK, 2017.
23. Wu, J.; Yang, F.; Zheng, J.C.; Nguyen, H.T.; Chai, R.F. Microwave Imaging Based on a Subspace-based Two-step Iterative Shrinkage/Thresholding Method. In Proceedings of the 2023 45th Annual International Conference of the Ieee Engineering in Medicine & Biology Society, Sydney, Australia, 24–27 July 2023. [CrossRef]
24. Chen, X.D. Subspace-Based Optimization Method for Solving Inverse-Scattering Problems. *IEEE Trans. Geosci. Remote. Sens.* **2010**, *48*, 42–49. [CrossRef]
25. Taflove, A.; Hagness, S.C. *Computational Electrodynamics: The Finite-Difference Time-Domain Method*, 2nd ed.; Allen, T., Susan, C.H., Eds.; Artech House: Boston, MA, USA, 2000.
26. Abubakar, A.; van den Berg, P.M. The contrast source inversion method for location and shape reconstructions. *Inverse Probl.* **2002**, *18*, 495–510. [CrossRef]

27. Bioucas-Dias, J.M.; Figueiredo, M.A.T. A new TwIST: Two-step iterative shrinkage/thresholding algorithms for image restoration. *IEEE Trans. Image Process.* **2007**, *16*, 2992–3004. [CrossRef] [PubMed]
28. Willoughby, R.A. Solutions of Ill-Posed Problems (A. N. Tikhonov and V. Y. Arsenin). *SIAM Rev.* **1979**, *21*, 266–267. [CrossRef]
29. Carmeliet, P.; Jain, R.K. Angiogenesis in cancer and other diseases. *Nature* **2000**, *407*, 249–257. [CrossRef] [PubMed]
30. Lazebnik, M.; McCartney, L.; Popovic, D.; Watkins, C.B.; Lindstrom, M.J.; Harter, J.; Sewall, S.; Magliocco, A.; Booske, J.H.; Okoniewski, M.; et al. A large-scale study of the ultrawideband microwave dielectric properties of normal breast tissue obtained from reduction surgeries. *Phys. Med. Biol.* **2007**, *52*, 2637–2656. [CrossRef]
31. Burfeindt, M.J.; Colgan, T.J.; Mays, R.O.; Shea, J.D.; Behdad, N.; Veen, B.D.V.; Hagness, S.C. MRI-Derived 3-D-Printed Breast Phantom for Microwave Breast Imaging Validation. *IEEE Antennas Wirel. Propag. Lett.* **2012**, *11*, 1610–1613. [CrossRef] [PubMed]
32. Colgan, T.J.; Hagness, S.C.; Van Veen, B.D. A 3-D Level Set Method for Microwave Breast Imaging. *IEEE Trans. Biomed. Eng.* **2015**, *62*, 2526–2534. [CrossRef] [PubMed]
33. Nguyen, P.T.; Abbosh, A.; Crozier, S. Microwave Hyperthermia for Breast Cancer Treatment Using Electromagnetic and Thermal Focusing Tested on Realistic Breast Models and Antenna Arrays. *IEEE Trans. Antennas Propag.* **2015**, *63*, 4426–4434. [CrossRef]